Switching Active Disturbance Rejection Based Deadbeat Predictive Current Control for Permanent Magnet Synchronous Motors

Zhengjie Hao, Yang Yang, Keyong Shao, and Yuanhong Liu

***Abstract*—To enhance prediction precision and tracking performance of current controllers for permanent magnet synchronous motor (PMSM) drives subject to control delay and disturbances, a switching active disturbance rejection based deadbeat predictive current control (SADR-DPCC) strategy of the PMSM is presented in this article. First, a traditional DPCC strategy is introduced based on the dynamic model of the PMSM and the parameter sensitivity of the DPCC is analyzed. Then, an active disturbance rejection based DPCC (ADR-DPCC) strategy is presented to alleviate the influence of disturbances on the DPCC controller. However, the ADR-DPCC only with the linear extended state observer (LESO) is incompetent in the applications with high requirement of control accuracy and robustness. Therefore, the SADR-DPCC strategy of the PMSM is proposed to integrate the advantages of the LESO and nonlinear extended state observer (NLESO) with a hysteretic switching strategy. Moreover, the stability analysis and parameter setting of the NLESO are elaborated, which are simplified by the switching strategy of the SADR-DPCC. Finally, the effectiveness and superiority of the SADR-DPCC are validated experimentally.**

***Index Terms*—Deadbeat predictive current control (DPCC), extended state observer (ESO), permanent magnet synchronous motor (PMSM), switching active disturbance rejection control (SADRC).**

I. Introduction

PERMANENT magnet synchronous motor (PMSM) drives have wide applications in the domain of frequency conversion drives such as rail transit traction and new energy vehicles due to the merits of good reliability, convenient maintenance, high efficiency, and power density [1], [2], [3]. Under normal operation conditions, the ratio of inverter switching frequency to motor running frequency is high to achieve outstanding dynamic performance and stability by adopting the classical PI controller in the current loop of the PMSM. However, the inverter is required to work at the lowest possible switching frequency to mitigate the power dissipation of switching components and reduce the radiator volume in the application of electric vehicles and high-power drives, the current loop of which is prone to oscillation and instability because the current control delay is increased with the decrease of converter switching frequency [4], [5]. Correspondingly, the system coupling is aggravated and the phase margin is reduced. Thus, a predictive current control (PCC) strategy of the PMSM is proposed and has been widely concerned and studied due to the features of good dynamic performance and low current harmonic components [6], [7], [8], [9].

There are mainly two types of PCC methods at present. One is to adopt a cost function, which is evaluated according to eight different voltage vectors of a voltage source inverter. Then, one of the voltage vectors is selected as the input voltage of the PMSM based on the principle of cost optimization, which is simple in design [10]. However, the control error of one-vector model predictive control (MPC) is large with only eight voltage vectors, which cannot achieve satisfactory control accuracy and current harmonic components. To overcome this deficiency, two-vector and three-vector MPC methods are presented in succession [11], [12], [13], [14], [15]. The other is to sample the stator current of the present control period and calculate the corresponding reference voltage of the next control period based on the PMSM model. Then, the voltage vector is synthesized by the space vector pulse width modulation (SVPWM) so that the output stator current of the next control period is equal to the reference stator current. The deadbeat PCC (DPCC) can achieve excellent dynamic performance and low current harmonics [16], [17], [18].

Nevertheless, an accurate PMSM model is essential to the DPCC strategy, but the PMSM is a typical nonlinear multivariable time-varying system and its stator resistance and permanent magnet flux are sensitive to temperature. Moreover, the discrete PMSM model equation is an approximate discrete linearization of the nonlinear model equation, and neglecting high-order terms can introduce model errors [19], [20]. In this way, the predictive reference voltage calculated by the nominal model equation deviates from the actual required voltage so the high current accuracy cannot be guaranteed. Therefore, the key of high-precision PCC is to obtain the compensation of model

Manuscript received 30 March 2023; revised 4 July 2023; accepted 18 August 2023. Date of publication 24 August 2023; date of current version 22 September 2023. This work was supported in part by the Northeast Petroleum University Talent Introduction and Research Initiation Funding Project 2022KQ15 and in part by the Northeast Petroleum University Electrical Youth Top Talent Fund Support Program under Grant DQKY202302. Recommended for publication by Associate Editor R. Kennel. *(Corresponding author: Yang Yang.)*

Zhengjie Hao, Keyong Shao, and Yuanhong Liu are with the School of Electrical and Information Engineering, Northeast Petroleum University, Daqing 163319, China (e-mail: haozj_nepu@163.com; shaokeyongauto@163.com; liuyuanhong@nepu.edu.cn).

Yang Yang is with the College of Physics, Jilin University, Changchun 130012, China (e-mail: jlu_yang@jlu.edu.cn).

Color versions of one or more figures in this article are available at https://doi.org/10.1109/TPEL.2023.3308167.

Digital Object Identifier 10.1109/TPEL.2023.3308167

errors. In [21], an observer-based robust PCC method is proposed for PMSMs which utilizes an extended state observer (ESO) to observe and compensate disturbances and currents with an augmented system model. However, the filtering effects have less influence on the low-order harmonics by virtue of the limited observer bandwidth. In [22], a DPCC strategy founded upon the enhanced predictive model and exponential ESO is presented for PMSMs to augment robustness and transient performance. However, in consideration of the system inertial element, the robustness analysis still lacks the speed predictive model in the discrete domain. An extended sliding mode observer (SMO) with Hurwitz-based power reaching law is presented in [23] for PMSMs to enhance the performance and robustness of the PCC. In [24], a composite control strategy integrating a modified DPCC scheme with feedback compensation based on a disturbance observer is proposed to enhance the current performance of the PMSM with parameter mismatches and control delay. In [25], an ameliorative DPCC controller for PMSMs with a composite SMO is presented to enhance the current accuracy and robustness of parameter mismatches. A static-errorless DPCC with the SMO is presented in [26] to handle static current errors and parameter mismatches. The SMO is designed to estimate the disturbances including parameter variation and system nonlinearity, which can effectively alleviate the chattering effect by the switching control. However, the SMOs in [23], [24], [25], and [26] inevitably result in jittering in the observation. A robust PCC strategy for PMSMs is presented in [27], which utilizes an incremental system model to realize motor operation with unknown rotor flux. An ESO is adopted to augment inductance robustness and a traditional DPCC is improved for multistep prediction to compensate for the control delay and enhance the control accuracy. In [28], an improved DPCC for surfaced PMSMs based on a Luenberger disturbance observer is presented to enhance the tracking performance and transient response of the PMSM which has no chattering and less computation in comparison with the SMO. Although the Luenberger observer in [27] and [28] is widely utilized for its straightforward structure and easy effectuation, it cannot accurately estimate the system status when the parameters vary rapidly. In [29], an improved model-free PCC for surface-mounted PMSMs is presented to tackle the disturbance of parameter mismatches with an improved ESO, which can expeditiously compensate for the disturbances without the knowledge of motor parameters. An improved robust PCC based on online *dq*-axis inductance identification for five-phase PMSMs under open-circuit fault is proposed with a fault-tolerant model reference adaptive system in [30].

To further improve the current performance, robustness, and prediction accuracy of the PMSM, an improved switching active disturbance rejection based DPCC (SADR-DPCC) is proposed in this article. The major contributions of this article can be summarized as follows.

1) The proposed SADR-DPCC integrates a DPCC with a switching ESO (SESO) to simultaneously improve the current prediction accuracy and disturbance rejection performance, which is the core component of the switching active disturbance rejection control (SADRC). It is advantageous to realize the DPCC with fast dynamic response and low current harmonics.
2) Parameter mismatches and external disturbances of the PMSM are taken as the estimated total disturbances, which are substituted into the predictive current model of the PMSM and observed in real time by the SESO to enhance the prediction accuracy and robustness of the SADR-DPCC.
3) The performance of nonlinear ESO (NLESO) decreases seriously with the rise of estimated error [31]. The SESO in this article combines the linear ESO (LESO) and NLESO via an appropriate switching strategy, which not only possesses the merits of the LESO and NLESO but also overcomes their shortcomings.
4) Compared with the existing NLESO schemes, the proposed switching strategy simplifies the parameter tuning and stability analysis of the NLESO, making the controller design intuitive.

The rest of this article is organized as follows. Section II proposes the dynamic model of the PMSM on account of disturbances and introduces conventional DPCC. Moreover, the parameter sensitivity of the conventional DPCC is analyzed and the active disturbance rejection based DPCC (ADR-DPCC) is proposed based on the dynamic model to ameliorate conventional DPCC. Section III proposes the SADR-DPCC of the PMSM and its stability analysis and parameter tuning strategy are elaborated by theoretical analysis and simulation. Section IV verifies the feasibility and validity of the SADR-DPCC for the PMSM by comparative experiments with conventional DPCC and ADR-DPCC. Finally, Section V concludes this article.

II. DPCC Design for PMSM

A. Dynamic Model of the PMSM Considering Disturbances

The voltage equations of the surface-mounted PMSM in the synchronous rotating *dq* frames are expressed as follows [32]:

$$\begin{cases} u_d = L_{\mathrm{s}} p i_d + R_{\mathrm{s}} i_d - n_{\mathrm{p}} \omega_{\mathrm{m}} L_{\mathrm{s}} i_q \\ u_q = L_{\mathrm{s}} p i_q + R_{\mathrm{s}} i_q + n_{\mathrm{p}} \omega_{\mathrm{m}} \left(L_{\mathrm{s}} i_d + \psi_f \right) \end{cases} \tag{1}$$

where i_d and i_q are *dq*-axis currents, respectively, u_d and u_q are *dq*-axis voltages, respectively, L_{s} and R_{s} are motor stator inductance and phase resistance, respectively, n_{p} are motor pole pairs, ψ_f is permanent magnet flux, ω_{m} is mechanical angular speed, and p is time derivative operator. Equation (1) can be rewritten as a standard state space equation given by

$$p \begin{bmatrix} i_d \\ i_q \end{bmatrix} = \boldsymbol{A} \begin{bmatrix} i_d \\ i_q \end{bmatrix} + \boldsymbol{B} \begin{bmatrix} u_d \\ u_q \end{bmatrix} + \boldsymbol{C} \tag{2}$$

where

$$\boldsymbol{A} = \begin{bmatrix} -R_{\mathrm{s}}/L_{\mathrm{s}} & n_{\mathrm{p}}\omega_{\mathrm{m}} \\ -n_{\mathrm{p}}\omega_{\mathrm{m}} & -R_{\mathrm{s}}/L_{\mathrm{s}} \end{bmatrix}, \ \boldsymbol{B} = \begin{bmatrix} 1/L_{\mathrm{s}} & 0 \\ 0 & 1/L_{\mathrm{s}} \end{bmatrix},$$

$$\boldsymbol{C} = \begin{bmatrix} 0 \\ -n_{\mathrm{p}}\omega_{\mathrm{m}}\psi_f/L_{\mathrm{s}} \end{bmatrix}.$$

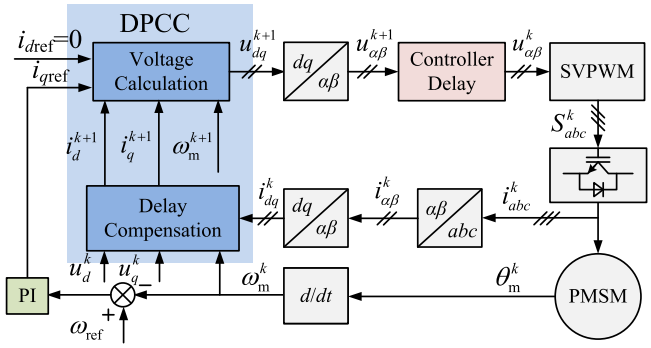

Fig. 1. Control block diagram of the PMSM drive system based on the traditional DPCC.

According to (1) and (2), the dynamic model of the PMSM taking parameter mismatches and external disturbances into account can be expressed as

$$p\begin{bmatrix} i_d \\ i_q \end{bmatrix} = \boldsymbol{A}^* \begin{bmatrix} i_d \\ i_q \end{bmatrix} + \boldsymbol{B}^* \begin{bmatrix} u_d \\ u_q \end{bmatrix} + \boldsymbol{C}^* + \begin{bmatrix} D_d \\ D_q \end{bmatrix} \tag{3}$$

where

$$\boldsymbol{A}^* = \begin{bmatrix} -R_{\mathrm{s}}^*/L_{\mathrm{s}}^* & n_{\mathrm{p}}\omega_{\mathrm{m}} \\ -n_{\mathrm{p}}\omega_{\mathrm{m}} & -R_{\mathrm{s}}^*/L_{\mathrm{s}}^* \end{bmatrix},\ \boldsymbol{B}^* = \begin{bmatrix} 1/L_{\mathrm{s}}^* & 0 \\ 0 & 1/L_{\mathrm{s}}^* \end{bmatrix},$$
$$\boldsymbol{C}^* = \begin{bmatrix} 0 \\ -n_{\mathrm{p}}\omega_{\mathrm{m}}\psi_f^*/L_{\mathrm{s}}^* \end{bmatrix}$$

L_{s}^*, R_{s}^* and ψ_f^* being the nominal stator inductance, phase resistance, and permanent magnet flux, respectively, and D_d and D_q are total disturbances of dq-axis currents, respectively, which can be expressed as

$$\begin{cases} D_d = D_{d\mathrm{in}} + D_{d\mathrm{ex}} \\ \quad = \left[\left(n_{\mathrm{p}}\omega_{\mathrm{m}} i_q - p i_d\right)\Delta L_{\mathrm{s}} - \Delta R_{\mathrm{s}} i_d\right]/L_{\mathrm{s}}^* + D_{d\mathrm{ex}} \\ D_q = D_{q\mathrm{in}} + D_{q\mathrm{ex}} \\ \quad = \left[-\left(n_{\mathrm{p}}\omega_{\mathrm{m}} i_d + p i_q\right)\Delta L_{\mathrm{s}} - \Delta R_{\mathrm{s}} i_q \right. \\ \qquad \left. -n_{\mathrm{p}}\omega_{\mathrm{m}}\Delta\psi_f\right]/L_{\mathrm{s}}^* + D_{q\mathrm{ex}} \end{cases} \tag{4}$$

where $\Delta L_{\mathrm{s}} = L_{\mathrm{s}} - L_{\mathrm{s}}^*$, $\Delta R_{\mathrm{s}} = R_{\mathrm{s}} - R_{\mathrm{s}}^*$, $\Delta\psi_f = \psi_f - \psi_f^*$, $D_{d\mathrm{in}}$ and $D_{q\mathrm{in}}$ are the dq-axis internal disturbances, respectively, mainly containing motor parameter variation, and $D_{d\mathrm{ex}}$ and $D_{q\mathrm{ex}}$ are the dq-axis external disturbances, respectively, reflected in step change of the reference currents.

B. Conventional DPCC

The control block diagram of the PMSM drive system based on conventional DPCC is shown in Fig. 1, where $i_{d\mathrm{ref}}$ and $i_{q\mathrm{ref}}$ are dq-axis reference currents, respectively, θ_{m} is rotor mechanical angle, and superscript "k" represents the corresponding state variable at kT_{s} where T_{s} is the control period. In virtue of the controller delay, the output voltage obtained at kT_{s} will drive the PMSM at $(k+1)T_{\mathrm{s}}$ so that the delay compensation module is utilized in the DPCC to compensate the controller delay. Specifically, the sampled current and applied voltage at kT_{s} are used to calculate the predictive current i_d^{k+1} and i_q^{k+1}, then on this basis, the predictive output voltage u_d^{k+1} and u_q^{k+1} required can be obtained.

The dq-axis currents at $t \in [kT_{\mathrm{s}}, (k+1)T_{\mathrm{s}}]$ can be obtained by solving (2) as

$$\begin{bmatrix} i_d(t) \\ i_q(t) \end{bmatrix} = \mathrm{e}^{(t-kT_{\mathrm{s}})\boldsymbol{A}} \begin{bmatrix} i_d(kT_{\mathrm{s}}) \\ i_q(kT_{\mathrm{s}}) \end{bmatrix} + \left[\mathrm{e}^{(t-kT_{\mathrm{s}})\boldsymbol{A}} - \boldsymbol{I}\right]\boldsymbol{A}^{-1}\boldsymbol{C} + \int_{kT_{\mathrm{s}}}^{t} \mathrm{e}^{(t-\tau)\boldsymbol{A}}\boldsymbol{B}\begin{bmatrix} u_d(\tau) \\ u_q(\tau) \end{bmatrix} d\tau \tag{5}$$

where $\boldsymbol{I}$ is the identity matrix.

The form of (5) is so complicated that it is inconvenient for practical application. The off-diagonal elements in matrix $\boldsymbol{A}$ contain ω_{m}, and $n_{\mathrm{p}}\omega_{\mathrm{m}}T_{\mathrm{s}}$ is very small when the ratio of control frequency to motor running frequency is high. Thus, they can be obtained as

$$\mathrm{e}^{(t-kT_{\mathrm{s}})\boldsymbol{A}} \approx (t-kT_{\mathrm{s}})\boldsymbol{A} + \boldsymbol{I} \tag{6}$$

$$\omega_{\mathrm{e}}(t-kT_{\mathrm{s}}) \approx 0. \tag{7}$$

Moreover, $u_d(t)$ and $u_q(t)$ at $t \in [kT_{\mathrm{s}}, (k+1)T_{\mathrm{s}}]$ can be written as

$$\begin{bmatrix} u_d(t) \\ u_q(t) \end{bmatrix} = \begin{bmatrix} \cos\omega_{\mathrm{e}}(t-kT_{\mathrm{s}}) & \sin\omega_{\mathrm{e}}(t-kT_{\mathrm{s}}) \\ -\sin\omega_{\mathrm{e}}(t-kT_{\mathrm{s}}) & \cos\omega_{\mathrm{e}}(t-kT_{\mathrm{s}}) \end{bmatrix} \begin{bmatrix} u_d(kT_{\mathrm{s}}) \\ u_q(kT_{\mathrm{s}}) \end{bmatrix}. \tag{8}$$

Substituting (7) into (8) gives

$$\begin{bmatrix} u_d(t) \\ u_q(t) \end{bmatrix} = \begin{bmatrix} 1 & \omega_{\mathrm{e}}(t-kT_{\mathrm{s}}) \\ -\omega_{\mathrm{e}}(t-kT_{\mathrm{s}}) & 1 \end{bmatrix} \begin{bmatrix} u_d(kT_{\mathrm{s}}) \\ u_q(kT_{\mathrm{s}}) \end{bmatrix}. \tag{9}$$

Substituting (6) and (9) into (5) gives

$$\begin{bmatrix} i_d(t) \\ i_q(t) \end{bmatrix} = \left[(t-kT_{\mathrm{s}})\boldsymbol{A} + \boldsymbol{I}\right]\begin{bmatrix} i_d(kT_{\mathrm{s}}) \\ i_q(kT_{\mathrm{s}}) \end{bmatrix} + (t-kT_{\mathrm{s}})\boldsymbol{C} + (t-kT_{\mathrm{s}})\boldsymbol{B}\begin{bmatrix} u_d(kT_{\mathrm{s}}) \\ u_q(kT_{\mathrm{s}}) \end{bmatrix}. \tag{10}$$

Both the delay compensation and predictive current calculation depend on the discrete form of (10) for the DPCC. In view of (10), the discrete form of dq-axis currents at $(k+1)T_{\mathrm{s}}$ can be expressed as

$$\begin{bmatrix} i_d^{k+1} \\ i_q^{k+1} \end{bmatrix} = (T_{\mathrm{s}}\boldsymbol{A} + \boldsymbol{I})\begin{bmatrix} i_d^k \\ i_q^k \end{bmatrix} + T_{\mathrm{s}}\boldsymbol{C} + T_{\mathrm{s}}\boldsymbol{B}\begin{bmatrix} u_d^k \\ u_q^k \end{bmatrix}. \tag{11}$$

According to (1) and (11), the output voltage of the PMSM DPCC can be obtained as

$$\begin{cases} u_d^{k+1} = \left(i_{d\mathrm{ref}} - i_d^{k+1}\right)L_{\mathrm{s}}/T_{\mathrm{s}} + R_{\mathrm{s}} i_d^{k+1} - n_{\mathrm{p}}\omega_{\mathrm{m}}^{k+1} L_{\mathrm{s}} i_q^{k+1} \\ u_q^{k+1} = \left(i_{q\mathrm{ref}} - i_q^{k+1}\right)L_{\mathrm{s}}/T_{\mathrm{s}} + R_{\mathrm{s}} i_q^{k+1} \\ \qquad + n_{\mathrm{p}}\omega_{\mathrm{m}}^{k+1}\left(L_{\mathrm{s}} i_d^{k+1} + \psi_f\right) \end{cases} \tag{12}$$

where $\omega_{\mathrm{m}}^{k+1} = \omega_{\mathrm{m}}^k$ because the control frequency is much higher than the motor running frequency.

Equations (11) and (12) are the discrete solutions of (2) obtained by the forward Euler approximation method and are mostly utilized by the existing DPCC to realize the delay compensation and predictive variables calculation. However,

the performance of traditional DPCC has a strong correlation with the precision of the PMSM mathematical model. In the practical operation process, the motor parameter variation and external disturbance have a strong influence on the PMSM drive system, resulting in increased prediction error so that it is difficult to realize precise tracking of the reference current [33].

C. Parameter Sensitivity Analysis

It can be seen from (12) that the traditional DPCC controller of the PMSM has high sensitivity to L_s, R_s, and ψ_f. The accuracy of the predictive model parameters has a significant influence on the control effect of the PMSM. To evaluate the impact of various parameter mismatches on predictive errors, the parameter sensitivity of the DPCC in the PMSM is analyzed.

According to (11), the discrete forms of dq-axis currents at $(k+1)T_s$ considering the parameter mismatch can be written as

$$\begin{bmatrix} \tilde{i}_d^{k+1} \\ \tilde{i}_q^{k+1} \end{bmatrix} = (T_s \boldsymbol{A}^* + \boldsymbol{I}) \begin{bmatrix} i_d^k \\ i_q^k \end{bmatrix} + T_s \boldsymbol{C}^* + T_s \boldsymbol{B}^* \begin{bmatrix} u_d^k \\ u_q^k \end{bmatrix} \tag{13}$$

where $\tilde{i}_d$ and $\tilde{i}_q$ are dq-axis currents considering the parameter mismatch, respectively.

The error between the predictive currents in (11) and (13) can be expressed as

$$\begin{cases} \varepsilon_d = \frac{\Delta L_s R_s - L_s \Delta R_s}{L_s(\Delta L_s + L_s)} T_s i_d^k - \frac{\Delta L_s}{L_s(\Delta L_s + L_s)} T_s u_d^k \\ \varepsilon_q = \frac{\Delta L_s R_s - L_s \Delta R_s}{L_s(\Delta L_s + L_s)} T_s i_q^k - \frac{\Delta L_s}{L_s(\Delta L_s + L_s)} T_s u_q^k \\ \quad + \frac{\Delta L_s \psi_f - L_s \Delta \psi_f}{L_s(\Delta L_s + L_s)} T_s \omega_e^k \end{cases}. \tag{14}$$

Differentiating (14) gives

$$\begin{cases} \frac{\partial \varepsilon_d}{\partial \Delta L_s} = \frac{T_s\left[(R_s + \Delta R_s) i_d^k - u_d^k\right]}{(\Delta L_s + L_s)^2} \\ \frac{\partial \varepsilon_d}{\partial \Delta R_s} = -\frac{T_s i_d^k}{\Delta L_s + L_s} \\ \frac{\partial \varepsilon_d}{\partial \Delta \psi_f} = 0 \\ \frac{\partial \varepsilon_q}{\partial \Delta L_s} = \frac{T_s\left[(R_s + \Delta R_s) i_q^k - u_q^k - \omega_e^k(\psi_f + \Delta \psi_f)\right]}{(\Delta L_s + L_s)^2} \\ \frac{\partial \varepsilon_q}{\partial \Delta R_s} = -\frac{T_s i_q^k}{\Delta L_s + L_s} \\ \frac{\partial \varepsilon_q}{\partial \Delta \psi_f} = -\frac{T_s \omega_e^k}{\Delta L_s + L_s} \end{cases}. \tag{15}$$

Equations (14) and (15) indicate that the d-axis current is not affected by flux mismatch, but the q-axis current suffers. Meanwhile, both the dq-axis currents are disturbed by resistance and inductance deviations. On these grounds, the relationship among the dq-axis predictive current response errors and the parameter mismatches of stator inductance, resistance, and permanent magnet flux is attained by simulation, as shown in Fig. 2. The reference speed of the PMSM is set to 3000 r/min with no load and the parameters of the PMSM are set as presented in Table I. It can be seen that the inductance mismatch exerts a strong influence on the dq-axis predictive current errors, especially on the q-axis predictive current error. Due to the adoption of the $i_d = 0$ control scheme, the resistance mismatch does not affect the d-axis predictive current and it also has little effect on the q-axis predictive current error. Moreover, there is no coupling relationship between the d-axis predictive current and permanent magnet flux, but the flux mismatch has a significant effect on the q-axis predictive current error.

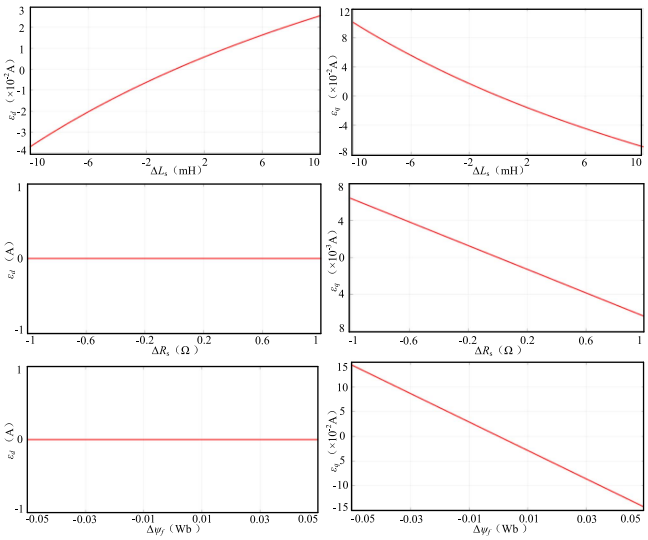

Fig. 2. Predictive current response errors under parameter mismatches. (a) d-axis. (b) q-axis.

TABLE I
MAIN NOMINAL PMSM PARAMETERS

Symbol	Specification	Value
n_p	Pole pairs	3
ψ_f	Permanent magnet flux	0.139 Wb
R_s	Stator phase resistance	3.1 Ω
L_s	Stator dq-axis inductances	51.3 mH
ω_N	Rated velocity	3000 r/min
T_N	Rated torque	0.48 N·m
I_N	Rated current	0.7 A
P_N	Rated power	170 W
V_{dc}	Rated dc bus voltage	310 V

Based on the above analysis, it can be concluded that the current control performance of the traditional DPCC strategy is highly sensitive to stator inductance, resistance, and permanent magnet flux. Hence, the robust design of the DPCC controller for the PMSM is supposed to be conducted.

D. ADR-DPCC

The ADRC can unify internal parameter perturbation and external disturbances into whole disturbances observed by the ESO, which is not dependent on a precise system model [34]. Due to the superior anti-interference capability of the ADRC, the ADR-DPCC of the PMSM is presented in this article to mitigate the influence of motor parameter variation and external disturbances on the DPCC.

According to (3), the discrete forms of dq-axis currents at $(k+1)T_s$ considering disturbances can be calculated in the

same way as

$$\begin{bmatrix} i_d^{k+1} \\ i_q^{k+1} \end{bmatrix} = (T_s \boldsymbol{A}^* + \boldsymbol{I}) \begin{bmatrix} i_d^k \\ i_q^k \end{bmatrix} + T_s \boldsymbol{C}^* + T_s \boldsymbol{B}^* \begin{bmatrix} u_d^k \\ u_q^k \end{bmatrix} + T_s \begin{bmatrix} D_d^k \\ D_q^k \end{bmatrix}. \tag{16}$$

As known from (16), it is essential to obtain dq-axis total disturbances at kT_s to predict the currents accurately. Hence, based on (3), two LESOs of dq-axis currents are designed to estimate the disturbance in real time as

$$\begin{cases} e_d = \hat{i}_d - i_d \\ p\hat{i}_d = u_d/L_s^* + f_d + \hat{D}_d - \beta_{dl1} e_d \\ p\hat{D}_d = -\beta_{dl2} e_d \\ f_d = n_p \omega_m i_q - R_s^* i_d / L_s^* \end{cases} \tag{17}$$

$$\begin{cases} e_q = \hat{i}_q - i_q \\ p\hat{i}_q = u_q/L_s^* + f_q + \hat{D}_q - \beta_{ql1} e_q \\ p\hat{D}_q = -\beta_{ql2} e_q \\ f_q = -R_s^* i_q / L_s^* - n_p \omega_m i_d - n_p \omega_m \psi_f^* / L_s^* \end{cases} \tag{18}$$

where $\hat{i}_d$ and $\hat{i}_q$ are dq-axis observed currents, respectively, $\hat{D}_d$ and $\hat{D}_q$ are dq-axis observed total disturbances, respectively, β_{dl1} and β_{dl2} are the gains of d-axis LESO, and β_{ql1} and β_{ql2} are the gains of q-axis LESO.

According to (3) and (17), assuming $e_{Dx} = \hat{D}_x - D_x$,where x represents d and q, respectively, the differential of e_x and e_{Dx} can be described as

$$p \begin{bmatrix} e_x \\ e_{Dx} \end{bmatrix} = \boldsymbol{H_x} \begin{bmatrix} e_x \\ e_{Dx} \end{bmatrix} \tag{19}$$

where

$$\boldsymbol{H_x} = \begin{bmatrix} -\beta_{xl1} & 1 \\ -\beta_{xl2} & 0 \end{bmatrix}.$$

It can be seen from (19) that the stability of the LESO entirely depends on the eigenvalue λ_H of $\mathbf{H}_{\boldsymbol{x}}$, which can be obtained by

$$|\lambda_H \boldsymbol{I} - \boldsymbol{H_x}| = \begin{vmatrix} \lambda_H + \beta_{xl1} & -1 \\ \beta_{xl2} & \lambda_H \end{vmatrix} = \lambda_H^2 + \beta_{xl1}\lambda_H + \beta_{xl2} = 0. \tag{20}$$

As long as both of the eigenvalues or their real part are less than zero, that is to say, $\beta_{xl1} > 0$ and $\beta_{xl2} > 0$, (19) is asymptotically stable. Moreover, if the parameters of the LESO are tuned as the demand that λ_H equals the bandwidth ω_0 of the LESO, it can be attained in view of (20) that

$$\lambda_H^2 + \beta_{xl1}\lambda_H + \beta_{xl2} = (\lambda_H + \omega_0)^2. \tag{21}$$

Then, β_{xl1} and β_{xl2} can be tuned as

$$\beta_{xl1} = 2\omega_0, \ \beta_{xl2} = \omega_0^2. \tag{22}$$

Based on the observed currents $\hat{i}_d$ and $\hat{i}_q$ and disturbances $\hat{D}_d$ and $\hat{D}_q$, (16) can be rewritten as

$$\begin{bmatrix} i_d^{k+1} \\ i_q^{k+1} \end{bmatrix} = (T_s \boldsymbol{A}^* + \boldsymbol{I}) \begin{bmatrix} \hat{i}_d^k \\ \hat{i}_q^k \end{bmatrix} + T_s \boldsymbol{C}^* + T_s \boldsymbol{B}^* \begin{bmatrix} u_d^k \\ u_q^k \end{bmatrix} + T_s \begin{bmatrix} \hat{D}_d^k \\ \hat{D}_q^k \end{bmatrix}. \tag{23}$$

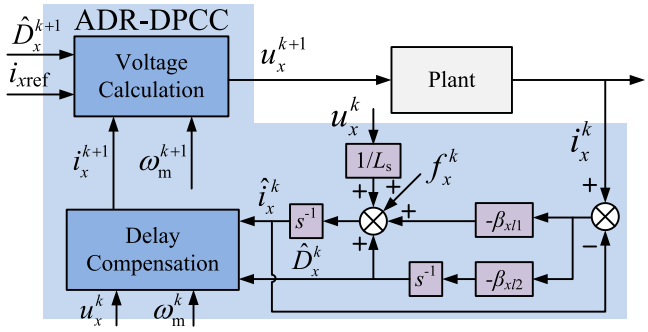

Fig. 3. Block diagram of the ADR-DPCC.

Then, the output voltages of the ADR-DPCC for the PMSM are expressed as

$$\begin{cases} u_d^{k+1} = \left(i_{dref} - i_d^{k+1}\right) L_s^*/T_s + R_s^* i_d^{k+1} \\ \qquad - n_p \omega_m^{k+1} L_s^* i_q^{k+1} - L_s^* \hat{D}_d^{k+1} \\ u_q^{k+1} = \left(i_{qref} - i_q^{k+1}\right) L_s^*/T_s + R_s^* i_q^{k+1} \\ \qquad + n_p \omega_m^{k+1} \left(L_s^* i_d^{k+1} + \psi_f^*\right) - L_s^* \hat{D}_q^{k+1} \end{cases} \tag{24}$$

where $\hat{D}_d^{k+1} = \hat{D}_d^k$ and $\hat{D}_q^{k+1} = \hat{D}_q^k$ because the motor parameter variation and external disturbances can be regarded as constant during extremely short current control period.

The block diagram of the ADR-DPCC for the PMSM is shown in Fig. 3. System disturbances caused by motor parameter mismatches and external disturbances can be observed in real time by the ADR-DPCC with the LESO, and the opportune disturbance compensation is provided, which enhances the robustness and prediction accuracy. Nevertheless, the ADR-DPCC only with the LESO is incompetent in the applications with high requirements of control accuracy and antidisturbance capability. The nonlinear ADRC (NLADRC) can be taken into consideration to further improve the control performance. However, complicated parameter tuning, stability analysis, and relatively slow response to large disturbances place restrictions on the application of the NLADRC for the DPCC of the PMSM [35]. To break the restrictions, the SADR-DPCC of the PMSM is proposed in the following section.

III. SADR-DPCC Design for PMSM

A. Proposed SADR-DPCC for the PMSM

According to (3), two ESOs of the SADR-DPCC for the PMSM can be designed, respectively, as follows:

$$\begin{cases} e_d = \hat{i}_d - i_d \\ p\hat{i}_d = u_d/L_s^* + f_d + \hat{D}_d - \beta_{d1}\varphi_{d1}(e_d) \\ p\hat{D}_d = -\beta_{d2}\varphi_{d2}(e_d) \\ f_d = n_p \omega_m i_q - R_s^* i_d / L_s^* \end{cases} \tag{25}$$

$$\begin{cases} e_q = \hat{i}_q - i_q \\ p\hat{i}_q = u_q/L_s^* + f_q + \hat{D}_q - \beta_{q1}\varphi_{q1}(e_q) \\ p\hat{D}_q = -\beta_{q2}\varphi_{q2}(e_q) \\ f_q = -R_s^* i_q / L_s^* - n_p \omega_m i_d - n_p \omega_m \psi_f^* / L_s^* \end{cases} \tag{26}$$

where β_{d1} and β_{d2} are the gains of d-axis ESO, and β_{q1} and β_{q2} are the gains of q-axis ESO. If $\varphi_{x1}(e_x)$ and $\varphi_{x2}(e_x)$ are selected as nonlinear functions, the ESO turns into an NLESO, which can be written as [31]

$$\varphi_{xi}(e_x) = \mathrm{fal}(e_x, \alpha_{xi}, \delta_x) = \begin{cases} \frac{e_x}{\delta_x^{1-\alpha_{xi}}} & |e_x| \le \delta_x \\ |e_x|^{\alpha_{xi}} \mathrm{sgn}(e_x) & |e_x| > \delta_x \end{cases} \tag{27}$$

where $i = 1, 2$, and α_{xi} and δ_x are indeterminate parameters. When $\alpha_{xi} < 1$, the nonlinear function possesses the characteristics of small gain with large deviation and high gain with small deviation, and δ_x stands for linear region to prevent the instability resulting from high gain with tiny error. Moreover, $\varphi_{x1}(e_x)$ and $\varphi_{x2}(e_x)$ can be set to e_x as well, and by this means, the ESO turns into an LESO.

Through the analysis of simulated mensuration, properties of the LESO and NLESO can be summarized below severally. Theoretical analysis and parameter setting of the LESO are simpler and its disturbance tracking ability cannot vary with the disturbance amplitude; the NLESO possesses the merits of superior tracking performance and estimation precision although the parameter tuning of the NLESO is more complex. In addition, the observation ability of the NLESO is relevant to disturbances, which is not entirely satisfactory under the condition of large disturbances.

Taking features of the LESO and NLESO into consideration, an idea is proposed that the ESO is chosen as the LESO with large disturbances while switching to the NLESO with small disturbances, which makes the most of two ESOs. Hence, a linear/nonlinear SESO is introduced.

To realize a smooth handoff in the SESO, a hysteretic switching scheme is presented, in which $\hat{i}_x$ and $\hat{D}_x$ are acquired by linear combinations of the LESO and NLESO, described, respectively, as

$$\hat{i}_x = \lambda_x \hat{i}_{xn} + (1 - \lambda_x)\, \hat{i}_{xl} \tag{28}$$

$$\hat{D}_x = \lambda_x \hat{D}_{xn} + (1 - \lambda_x)\, \hat{D}_{xl} \tag{29}$$

$$\lambda_x = \frac{a_x + b_x}{2} \tag{30}$$

$$a_x = \begin{cases} 1 & |e_x| \le e_{x1} \\ \frac{e_{x2} - |e_x|}{e_{x2} - e_{x1}} & e_{x1} < |e_x| < e_{x2} \\ 0 & |e_x| \ge e_{x2} \end{cases} \tag{31}$$

$$b_x = \begin{cases} 1 & \left|\hat{D}_x\right| \le D_{x1} \\ \frac{D_{x2} - \left|\hat{D}_x\right|}{D_{x2} - D_{x1}} & D_{x1} < \left|\hat{D}_x\right| < D_{x2} \\ 0 & \left|\hat{D}_x\right| \ge D_{x2} \end{cases} \tag{32}$$

where e_{x1} and e_{x2} are lower and upper limitations of estimated current error in the switchover process, respectively, D_{x1} and D_{x2} are lower and upper limitations of disturbances in the switchover process, respectively, $\hat{i}_{xn}$ and $\hat{i}_{xl}$ are the observed currents of the NLESO and LESO, respectively, and $\hat{D}_{xn}$ and $\hat{D}_{xl}$ are the observed disturbances of the NLESO and LESO, respectively. The observed currents and disturbances are acquired by means of switching two observers with hysteresis bands based on (28)–(32). By substituting them into (23) and (24), the output voltages of the SADR-DPCC for the PMSM are obtained, and its block diagram is shown in Fig. 4.

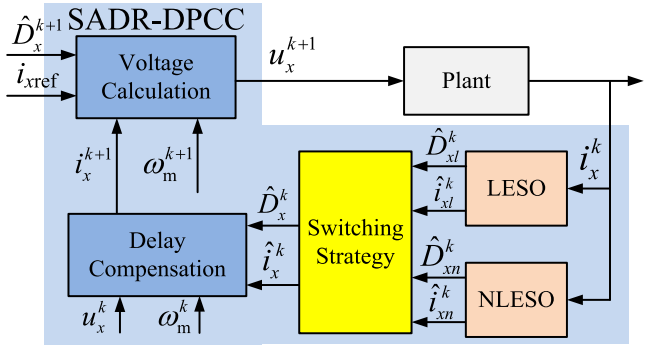

Fig. 4. Block diagram of the SADR-DPCC.

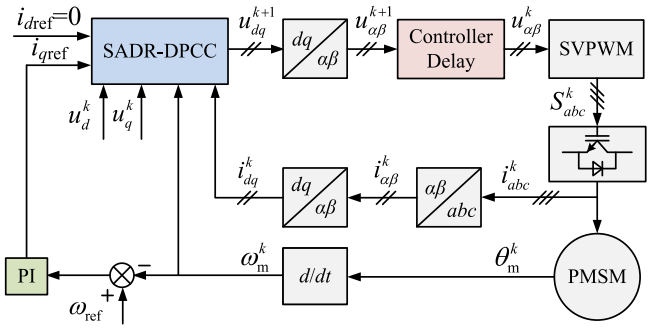

Fig. 5. Control block diagram of the PMSM drive system based on the SADR-DPCC.

The control block diagram of the PMSM drive system founded upon the presented SADR-DPCC strategy is shown in Fig. 5. The PI control scheme is utilized in the speed loop to generate the q-axis reference current. The SADR-DPCC is utilized in the current loop, which expeditiously compensates the various disturbances comprised of motor parameter variation and external disturbances through the nonlinear mechanism of fast response with large deviation and high gain with small deviation. The proposed SADR-DPCC strategy integrates the merits of the LESO and NLESO and evades their drawbacks by virtue of the proposed switching scheme, which augments the control precision and robustness of the PMSM.

B. Stability Analysis and Parameter Tuning for the NLESO

The stability analysis and parameter tuning of the LESO in the SADR-DPCC controller are elaborated in Section II-D, the difficulty of which lies in the NLESO. Until now, no systematic tuning method has been competent for the NLESO, mainly relying on practical experience. Nevertheless, the stability analysis and parameter setting of the NLESO in the SADR-DPCC controller are much simpler than that of the conventional NLESO because the operating state of the NLESO is circumscribed by the proposed switching scheme. Meanwhile, the stability of the NLESO can be analyzed by means of borrowing the bandwidth scheme of the LESO as well [36].

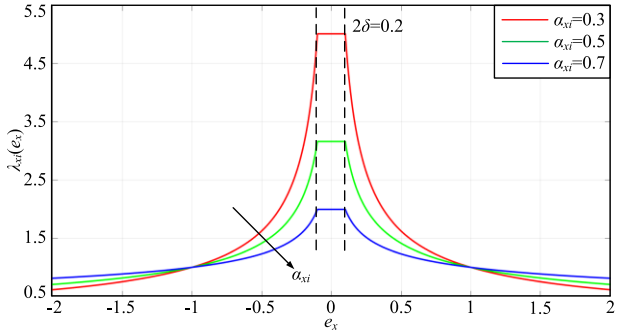

Fig. 6. Outputs of function $\lambda_{xi}(e_x)$ with different α_{xi}.

According to (25)–(27), α_{x1}, α_{x2}, β_{x1}, β_{x2}, and δ_x need to be tuned. The parameter tuning strategy is presented by researching the functional roles of indeterminate parameters in the NLESO and utilizing the bandwidth method.

Let

$$\text{fal}\left(e_x, \alpha_{xi}, \delta_x\right) = \frac{\text{fal}\left(e_x, \alpha_{xi}, \delta_x\right)}{e_x} e_x = \lambda_{xi}\left(e_x\right) e_x. \tag{33}$$

Substituting (33) into (25)–(27) gives

$$\begin{cases} e_x = \hat{i}_x - i_x \\ p\hat{i}_x = u_x/L_s^* + f_x + \hat{D}_x - \beta_{x1}\lambda_{x1}\left(e_x\right) e_x \\ p\hat{D}_x = -\beta_{x2}\lambda_{x2}\left(e_x\right) e_x \end{cases}. \tag{34}$$

The properties of $\lambda_{xi}(e_x)$ are researched below. The functions $\lambda_{xi}(e_x)$ with different α_{xi} are obtained for comparison in output change by choosing α_{xi} as 0.3, 0.5, and 0.7 severally, and δ_x is selected as 0.1, outputs of which are illustrated in Fig. 6. With the increase of α_{xi}, the nonlinearity of $\lambda_{xi}(e_x)$ decreases, and the maximum gain decreases as well. Thus, greatly small α_{xi} can lead to intensive oscillation of outputs, whereas large α_{xi} makes the NLESO unable to bring into play expeditious error attenuation and strong robustness. In other words, α_{xi} has a great impact on the observer. Moreover, $\lambda_{xi}(e_x)$ is invariant, whereas e_x is in the interval $[-\delta_x,\ \delta_x]$, and $(\lambda_{xi})_{\max} = \delta_x^{\alpha_{xi}-1}$. When $|e_x| > \delta_x$, $\lambda_{xi}(e_x)$ decreases with the increase of $|e_x|$, which achieves nonlinear properties of small gain with large deviation and high gain with small deviation. With regard to the SESO, when $|e_x| > 1$, $\lambda_{xi}(e_x) < 1$, namely small gain leading to slow response, so e_{x1} and e_{x2} of the proposed switching strategy are set to 1 and 1.2, respectively, which are proper as the switching thresholds. Meanwhile, D_{x1} and D_{x2} are supposed to be set to $20\%\hat{L}_s u_{x\max}$ and $25\%\hat{L}_s u_{x\max}$, respectively, where $u_{x\max}$ is the maximum x-axis voltage. Furthermore, it can be deduced from Fig. 6 that large δ_x can result in the invalidation of nonlinear characteristics, whereas small δ_x can make the NLESO violently oscillatory. Ordinarily, δ_x ought to be in the interval [0.01, 0.1], and $\delta_x = 0.05$ is appropriate in the SADR-DPCC controller of the PMSM; α_{xi} should satisfy the condition of $\alpha_{x1} > \alpha_{x2}$, and α_{x1} and α_{x2} can be set to empirical values of 0.5 and 0.25, respectively.

Based on (34), the NLESO can be regarded as a LESO with varying parameters, which are $\beta_{xi}\lambda_{xi}(e_x)$. Then, imitating the stability analysis of the LESO, the differential of e_x and e_{Dx} can be expressed as

$$p\begin{bmatrix} e_x \\ e_{Dx} \end{bmatrix} = \boldsymbol{S_x}\begin{bmatrix} e_x \\ e_{Dx} \end{bmatrix} \tag{35}$$

where

$$\boldsymbol{S_x} = \begin{bmatrix} -\beta_{x1}\lambda_{x1}\left(e_x\right) & 1 \\ -\beta_{x2}\lambda_{x2}\left(e_x\right) & 0 \end{bmatrix}.$$

Therefore, the stability of the NLESO entirely depends on the eigenvalue λ_S of $\boldsymbol{S_x}$, which can be obtained by

$$\begin{aligned} \left|\lambda_S \boldsymbol{I} - \boldsymbol{S_d}\right| &= \begin{vmatrix} \lambda_S + \beta_{x1}\lambda_{x1}\left(e_x\right) & -1 \\ \beta_{x2}\lambda_{xx}\left(e_x\right) & \lambda_S \end{vmatrix} \\ &= \lambda_S^2 + \beta_{x1}\lambda_{x1}\left(e_x\right)\lambda_S + \beta_{x2}\lambda_{xx}\left(e_x\right) = 0. \end{aligned} \tag{36}$$

As long as both of the eigenvalues or their real part are less than zero, the NLESO can be proved to be asymptotically stable. According to (36), the conditions of stability are obtained as

$$\beta_{x1}\lambda_{x1}\left(e_x\right) > 0,\ \beta_{x2}\lambda_{x2}\left(e_x\right) > 0. \tag{37}$$

Furthermore, it can be obtained owing to the switching strategy of the ADRC-DPCC that

$$\lambda_{x1}(e_x)_{\min} = \lambda_{x2}(e_x)_{\min} = 1. \tag{38}$$

Substituting (38) into (37) yields

$$\beta_{x1}\lambda_{x1}\left(e_x\right) \geq \beta_{x1} > 0,\ \beta_{x2}\lambda_{x2}\left(e_x\right) \geq \beta_{x2} > 0. \tag{39}$$

Hence, the stability conditions of the NLESO are the same as that for the LESO. That is to say, provided $\beta_{x1} > 0$ and $\beta_{x2} > 0$ are satisfied, the NLESO is asymptotically stable.

In the SADR-DPCC controller, the LESO is adopted to observe and compensate for large disturbances, whereas the NLESO is just applied in the case of small disturbances. Consequently, the current control period and interference are significant factors to be taken into account in the process of tuning parameters β_{x1} and β_{x2}. Although the dynamic performance of the NLESO is augmented with a proper increase in β_{x2}, overshooting and instability of whole disturbances estimation are generated easily, which deteriorates stability of the NLESO, and small β_{x2} can also attenuate the response of the observer to disturbances. Therefore, based on the parameter tuning optimization in [35],β_{x1} and β_{x2} can be written as, respectively,

$$\beta_{\mathrm{x1}} = 3\omega_0,\ \beta_{x2} = \frac{3\omega_0^2}{5}. \tag{40}$$

Obviously, (40) always meets the stability conditions of the NLESO for any ω_0 greater than zero, which also embodies the effectiveness of the switching strategy in the SADR-DPCC controller. Nevertheless, ω_0 still has an impact on the NLESO. By reorganizing the Laplace transform of (34), the transfer function of the observed current $\hat{i}_x$ can be expressed as

$$\begin{aligned} \hat{i}_x = &\frac{s\beta_{x1}\lambda_{x1}\left(e_x\right) + \beta_{x2}\lambda_{x2}\left(e_x\right)}{s^2 + \beta_{x1}\lambda_{x1}\left(e_x\right)s + \beta_{x2}\lambda_{x2}\left(e_x\right)} i_x \\ &+ \frac{su_x/\hat{L}_s + sf_x}{s^2 + \beta_{x1}\lambda_{x1}\left(e_x\right)s + \beta_{x2}\lambda_{x2}\left(e_x\right)}. \end{aligned} \tag{41}$$

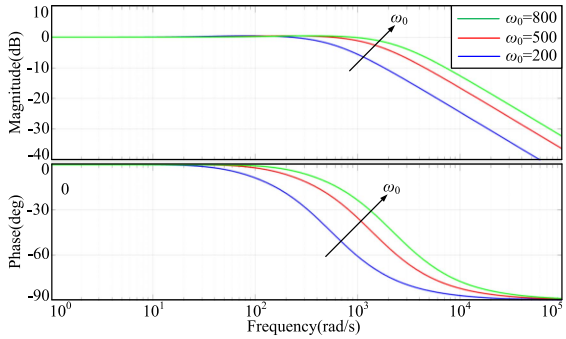

Fig. 7. Frequency analysis of observed currents with different ω_0.

Equation (41) indicates that the influence of ω_0 on the disturbance rejection ability to disturbances of u_x and f_x is apparent, which is augmented with the increase in ω_0, whereas the analysis of disturbance rejection ability to disturbance with regard to i_x is complicated. Therefore, to facilitate the analysis, disturbances of u_x and f_x and nonlinearity are neglected; in other words, $u_x = 0$, $f_x = 0$, $\lambda_{x1}(e_x) = \lambda_{x2}(e_x) = 1$, and (40) are substituted into (41), which can be rewritten as

$$\frac{\hat{i}_x}{i_x} = \frac{3\omega_0 s + 0.6\omega_0^2}{s^2 + 3\omega_0 s + 0.6\omega_0^2}. \tag{42}$$

The frequency domain characteristics of observed currents are shown in Fig. 7, with different ω_0 selected as 200, 500, and 800 severally. With the increase in ω_0, the transient performance of the observer is improved, concretely reflected by faster convergence speed of observation error, higher accuracy, and less phase lag of observed current. Nevertheless, the influence of high-frequency interference with large ω_0 ought not to be neglected, resulting in the deterioration of current prediction accuracy. Thus, ω_0 is supposed to be tuned by increasing slowly until the current estimation accuracy of the SADR-DPCC controller meets the requirements.

IV. Experimental Results

A. Experimental Setup

To further demonstrate the feasibility and validity of the proposed strategy for PMSMs, the SADR-DPCC, ADR-DPCC, and conventional DPCC control strategies are conducted for comparison at a laboratory platform, as shown in Fig. 8. Main nominal parameters of the prototype are given in Table I, which can change under different operation conditions. The temperature and current amplitude have a strong influence on the parameters of the PMSM, causing actual parameters to deviate from nominal parameters, and the error from that can be corrected by the proposed SADR-DPCC strategy. In the platform, the load torque of the PMSM is generated by a mechanically coupled load dynamometer. The control programs are executed by R5F24T8ADFM MCU and the prototype is driven by SCM1272MF IPM. Moreover, both the current control frequency and inverter switching frequency are set to 2 kHz. A quadrature encoder is utilized to obtain the position information of the prototype. Moreover, the

1:PMSM 2:Dynamometer 3:Dynamometer controller 4:Control board 5:Communication device 6:Isolation transformer 7:PC

Fig. 8. Experimental setup for verifying the presented SADR-DPCC strategy.

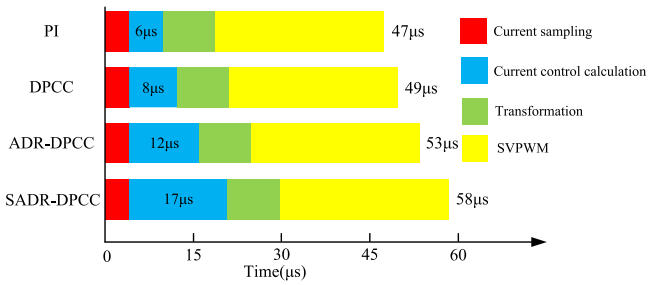

Fig. 9. Execution times of different control strategies.

gains of the SADR-DPCC and ADR-DPCC are the same based on the parameter setting method in Section III-B, which are set as $\beta_{d1} = \beta_{q1} = \beta_{dl1} = \beta_{ql1} = 1.8 \times 10^3$, and $\beta_{d2} = \beta_{q2} = \beta_{dl2} = \beta_{ql2} = 2.16 \times 10^5$, and the other parameters of the SADR-DPCC are tuned as $\alpha_{d1} = \alpha_{q1} = 0.5$, $\alpha_{d2} = \alpha_{q2} = 0.25$, and $\delta_d = \delta_q = 0.05$. The parameters of the PI controller in the speed loop are corrected as $k_{\text{sp}} = 1.344$ and $k_{\text{si}} = 0.27$ and the current loop parameters are selected as $k_{\text{cp}} = 32.76$ and $k_{\text{ci}} = 1920$ with the same bandwidth of the SADR-DPCC.

The execution times of different control strategies in R5F24T8ADFM MCU are shown in Fig. 9. The execution times of current sampling, transformation, and SVPWM are 4 μs, 9 μs, and 28 μs, respectively, which are the same in different control strategies. The main difference in the execution times in the PI, DPCC, ADR-DPCC, and SADR-DPCC strategies is the time used for current control calculation, which are 6 μs, 8 μs, 12 μs, and 17 μs, respectively. It can be obviously seen that all four strategies can be executed in one sampling period, which is 500 μs. Hence, the total execution time of the proposed strategy is slightly longer than those of the PI, DPCC, and ADRC-DPCC strategies, but it is totally worth adopting the SADR-DPCC due to significant performance improvement.

B. Speed Reversal Performance

The waveforms of the speeds, q-axis currents, and phase currents i_{a} in the PMSM based on conventional DPCC, ADR-DPCC, and SADR-DPCC are shown in Fig. 10; the given velocity is set to 1000 r/min first, and then set to -1000 r/min at 0.4 s, where Δt is the settling time and $\bar{e}_i$ is the average error of i_q

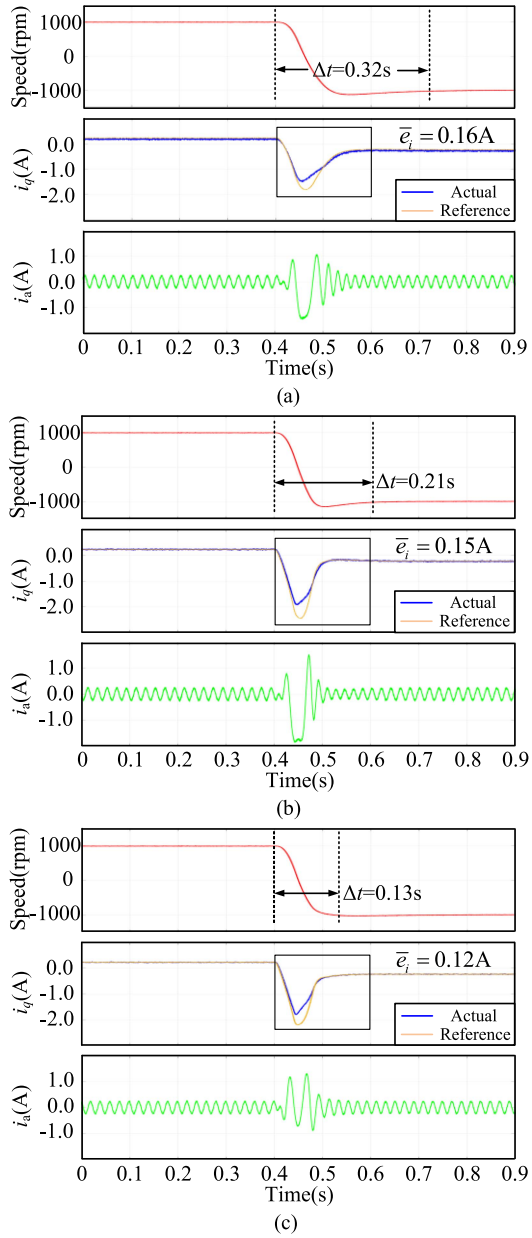

Fig. 10. Speed reversal performances of the PMSM. (a) DPCC. (b) ADR-DPCC. (c) SADR-DPCC.

TABLE II
SPEED REVERSAL PERFORMANCE COMPARISON

Metric	DPCC	ADR-DPCC	SADR-DPCC
Δt (s)	0.32	0.21	0.13
$\overline{e}_i$ (A)	0.16	0.15	0.12

during the transient of the speed reversal. The PMSM works with a constant load torque of 0.16 N·m. The contrastive experimental results of speed reversal performances are shown in Table II. This indicates clearly that the settling time of conventional DPCC is relatively longer, whereas the speed dynamics of the ADR-DPCC and SADR-DPCC are faster. Moreover, there is little difference between the average current errors of the DPCC and ADR-DPCC, but the ADR-DPCC can regulate the current faster. The current adjustment of the ADR-DPCC with large current deviation is as expeditious as the SADR-DPCC, but the current regulation of the SADR-DPCC with small current difference is better than the current regulation of ADR-DPCC so that the average current error of the SADR-DPCC is minimum. The settling times of conventional DPCC and ADR-DPCC are 146.15% and 61.54% slower than that of the SADR-DPCC, which confirms the excellent transient performance of the SADR-DPCC during speed reversal process.

TABLE III
STEADY-STATE PERFORMANCE COMPARISON

Metric	PI	DPCC	ADR-DPCC	SADR-DPCC
Δn (r/min)	36	33	18	12
Δi_q (A)	0.19	0.17	0.11	0.06
THD	12.84%	11.13%	8.7%	7.55%

C. Current Steady-State Performance

The reference velocity is regulated to 3000 r/min with a constant load torque of 0.48 N·m for the prototype. The waveforms of speeds, q-axis currents, phase currents i_a, and current harmonics are shown in Fig. 11, in comparison with the PI, conventional DPCC, ADR-DPCC, and SADR-DPCC methods, where Δn and Δi_q are speed and q-axis actual current fluctuation maximums, respectively. Experimental results of steady-state performances in the prototype adopting different control strategies are presented in Table III. It can be observed that the velocity, current fluctuations, and harmonics of the PI are all larger than those of the DPCC strategies, which reflects the good steady-state performance of the DPCC strategies with fewer current harmonics. Among the DPCC strategies, conventional DPCC has the largest velocity, current fluctuations, and harmonics, the ADR-DPCC has relatively smaller, and the SADR-DPCC has the smallest. Δn of conventional DPCC and ADR-DPCC are 175% and 50% larger than Δn of the SADR-DPCC, respectively, and Δi_q of conventional DPCC and ADR-DPCC are 183.33% and 83.33% larger than Δi_q of the SADR-DPCC, respectively. Moreover, phase current harmonics of the DPCC with the ESO are decreased compared to conventional DPCC. Current harmonics of the ADR-DPCC and SADR-DPCC make reductions of 21.83% and 32.17%, respectively, which validates the excellent steady-state performance of the presented SADR-DPCC in virtue of the feature of high gain with small deviation.

D. Current Dynamic Performance

The reference velocity is regulated invariably to 3000 r/min and the q-axis current reference is set from 0.9 to 1.4 A at 3 ms. The q-axis currents of the PI, traditional DPCC, ADR-DPCC, and SADR-DPCC strategies at a given state are shown in Fig. 12. The dynamic current regulation capability of the DPCC strategies is significantly superior to the PI control strategy. Moreover, the current overshoot of the DPCC and ADR-DPCC are both

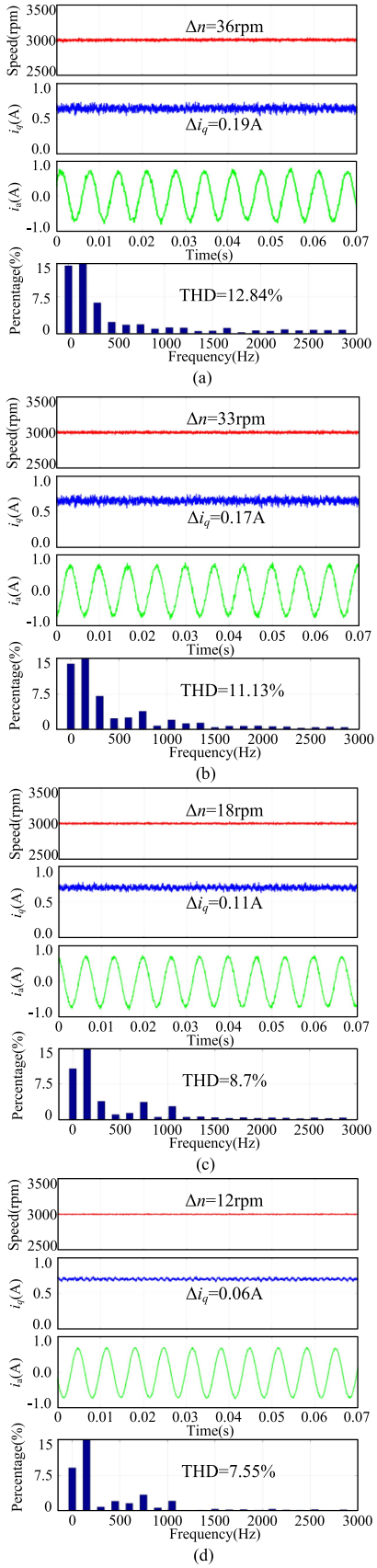

Fig. 11. Steady-state performances of the PMSM at 3000 r/min with a constant load torque of 0.48 N·m. (a) PI. (b) DPCC. (c) ADR-DPCC. (d) SADR-DPCC.

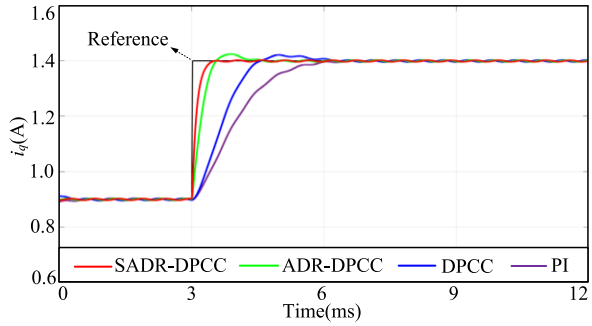

Fig. 12. Current dynamic performance comparison at 3000 r/min.

TABLE IV
ROBUSTNESS COMPARISON OF THE PMSM

Metric		DPCC	ADR-DPCC	SADR-DPCC
Δi_q/ Δi_d (A)	$3R_s$	0.31/0.2	0.22/0.13	0.07/0.06
	$0.3R_s$	0.24/0.17	0.16/0.11	0.06/0.06
	$3L_s$	0.39/0.43	0.27/0.23	0.09/0.07
	$0.3L_s$	0.22/0.21	0.17/0.12	0.06/0.06
	$3\psi_f$	0.27/0.16	0.21/0.11	0.1/0.07
	$0.3\psi_f$	0.19/0.17	0.14/0.1	0.05/0.06

larger than that of the SADR-DPCC due to the nonlinear characteristic of high gain with small deviation. Correspondingly, the settling time of the PI, DPCC, and ADR-DPCC are all slower than that of the SADR-DPCC. This indicates clearly that the current tracking performance of the PMSM adopting the SADR-DPCC is the best, which confirms the superior dynamic performance of the SADR-DPCC, with a tiny current overshoot and the shortest settling time.

E. Parameter Sensitivity

The reference velocity is regulated to 3000 r/min with a constant load torque of 0.48 N·m. The parameter mismatches are set at 0.5 s to verify the parameter sensitivity of the control strategies. The experimental results of reference and actual current responses with different parameter mismatches utilizing conventional DPCC, ADR-DPCC, and SADR-DPCC strategies are shown in Figs. 13–15, respectively, where Δi_q and Δi_d are q-axis and d-axis actual current fluctuation maximums, respectively. Actual current fluctuations after different added parameter mismatches of three control strategies are shown in Table IV. As shown in Fig. 13, parameter mismatches have a great influence on dq-axis current responses with regard to conventional DPCC. More specifically, the parameter mismatches of resistance and permanent magnet flux linkage can produce the static deviation between q-axis reference and actual currents of conventional DPCC. Moreover, the parameter mismatches of resistance, inductance, and permanent magnet flux can deteriorate the q-axis actual current fluctuation of conventional DPCC, and the effect of inductance mismatch is the worst. Not only that, the d-axis actual current of conventional DPCC also

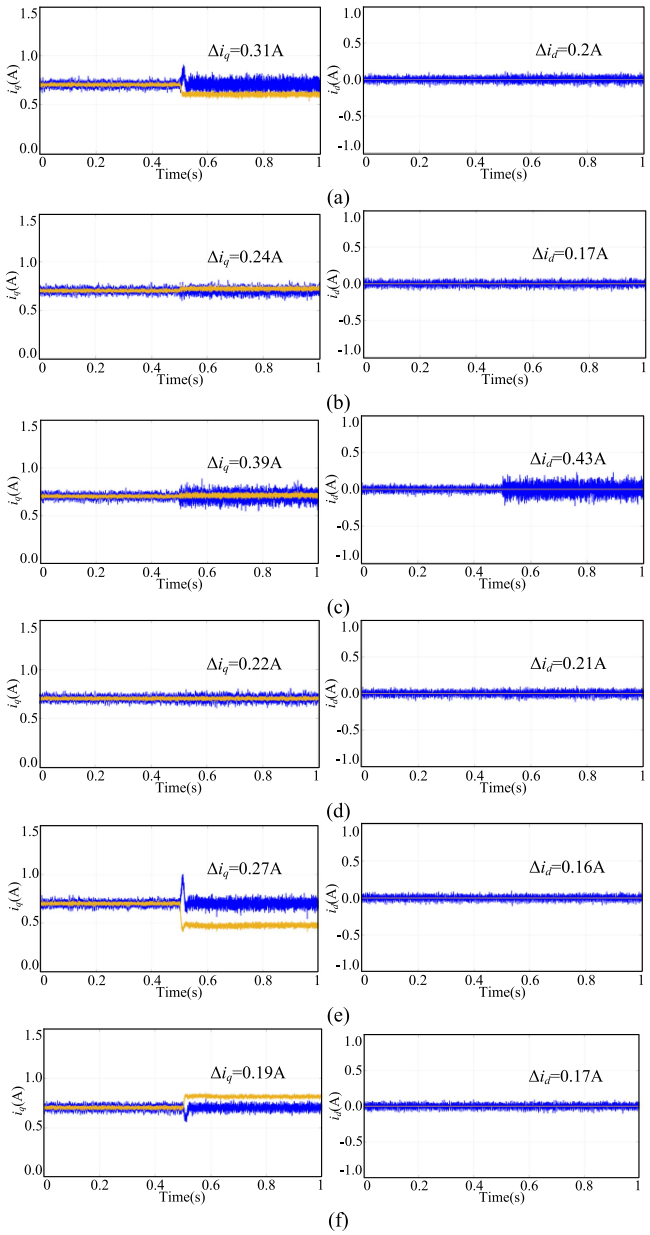

Fig. 13. Performances of conventional DPCC strategy under different parameter mismatch conditions where the orange lines represent reference currents and the blue lines represent actual currents. (a)$R_{\mathrm{s}}^{*}=3R_{\mathrm{s}}$. (b)$R_{\mathrm{s}}^{*}=0.3R_{\mathrm{s}}$. (c)$L_{\mathrm{s}}^{*}=3L_{\mathrm{s}}$. (d)$L_{\mathrm{s}}^{*}=0.3L_{\mathrm{s}}$. (e)$\psi_f^{*}=3\psi_f$. (f)$\psi_f^{*}=0.3\psi_f$.

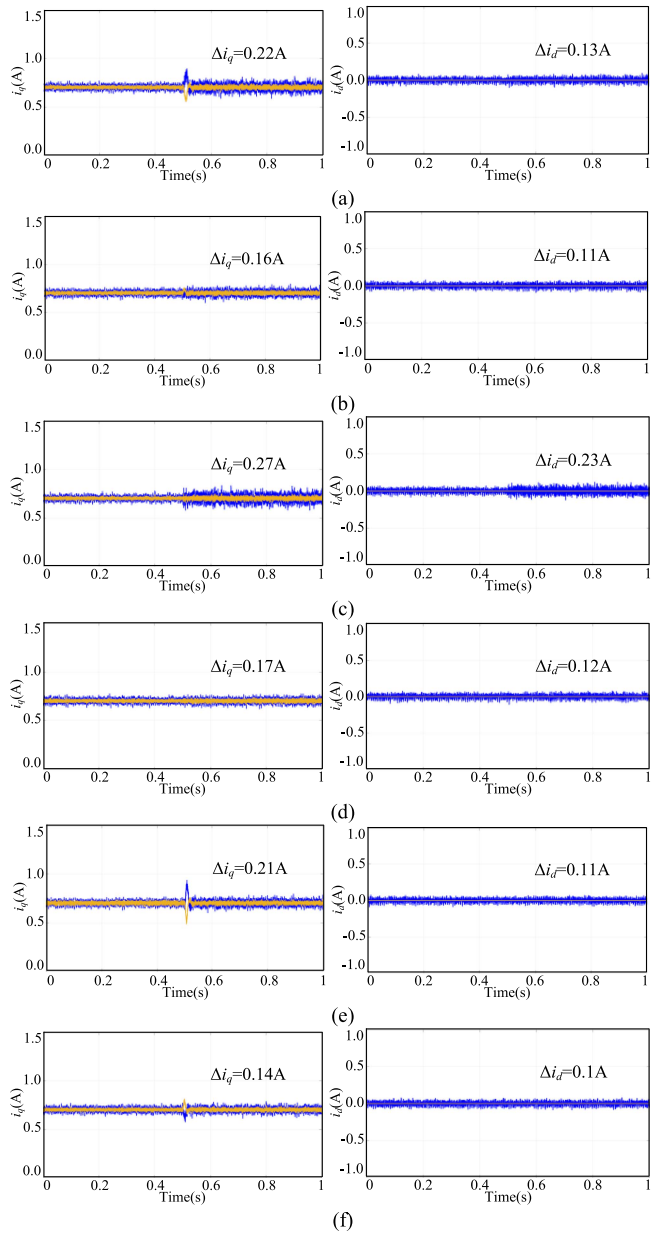

Fig. 14. Performances of the ADR-DPCC strategy under different parameter mismatch conditions where the orange lines represent reference currents and the blue lines represent actual currents. (a) $R_{\mathrm{s}}^{*}=3R_{\mathrm{s}}$. (b) $R_{\mathrm{s}}^{*}=0.3R_{\mathrm{s}}$. (c) $L_{\mathrm{s}}^{*}=3L_{\mathrm{s}}$. (d) $L_{\mathrm{s}}^{*}=0.3L_{\mathrm{s}}$. (e) $\psi_f^{*}=3\psi_f$. (f) $\psi_f^{*}=0.3\psi_f$.

suffers most from inductance mismatch but is slightly influenced by resistance mismatch, and permanent magnet flux mismatch has no influence on the *d*-axis actual current. As shown from Figs. 14 and 15, in comparison with conventional DPCC, the deviation between *q*-axis reference and actual currents by virtue of parameter mismatches is eliminated by the ADR-DPCC and SADR-DPCC strategies. The parameter mismatches are estimated and compensated by the ESOs in the ADR-DPCC and SADR-DPCC controllers. In addition, the *dq*-axis current fluctuations of them are much smaller than conventional DPCC. However, it can be clearly found that not only the *dq*-axis current fluctuations of the ADR-DPCC strategy are larger than those of the SADR-DPCC strategy, but also the sudden change of *q*-axis current in the ADR-DPCC controller is greater in the circumstances of the parameter mismatches of resistance and permanent magnet flux, which is detrimental to high precision current control of the PMSM. In the SADR-DPCC controller, the *dq*-axis current fluctuations have little difference before and after the parameter mismatches, embodying excellent robustness by means of the appropriate switching between the LESO and NLESO. Hence, comparative experiments of the SADR-DPCC, ADR-DPCC, and conventional DPCC strategies validate the superior robustness of motor parameters in the PMSM drive system with the SADR-DPCC.

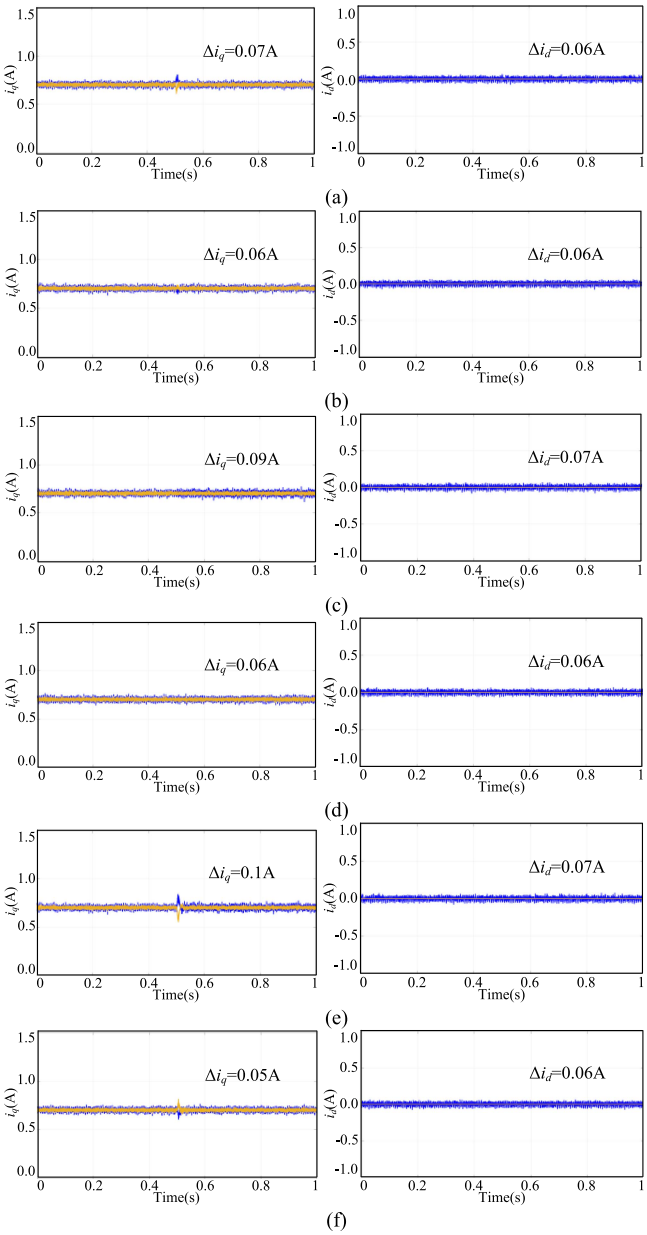

Fig. 15. Performances of the SADR-DPCC strategy under different parameter mismatch conditions where the orange lines represent reference currents and the blue lines represent actual currents. (a) $R_{\mathrm{s}}^{*} = 3R_{\mathrm{s}}$. (b) $R_{\mathrm{s}}^{*} = 0.3R_{\mathrm{s}}$. (c) $L_{\mathrm{s}}^{*} = 3L_{\mathrm{s}}$. (d) $L_{\mathrm{s}}^{*} = 0.3L_{\mathrm{s}}$. (e) $\psi_f^{*} = 3\psi_f$. (f) $\psi_f^{*} = 0.3\psi_f$.

V. Conclusion

A SADR-DPCC strategy for the PMSM drive system is presented to improve the dynamic performance, robustness, and prediction accuracy. Conventional DPCC is introduced first, which is extremely sensitive to the parameters of the PMSM, and the parameter sensitivity of the DPCC is analyzed. Then, the ADR-DPCC is proposed to improve the robustness but is still unsatisfied with the requirement of high control accuracy. The proposed SADR-DPCC scheme incorporates the nonlinear mechanism of the SADRC into the DPCC to achieve the characteristics of high gain with small deviation and fast response with large deviation, which overcomes drawbacks of conventional DPCC and ADR-DPCC. The smooth handoff between the LESO and NLESO is realized by the proposed hysteretic switching strategy. Moreover, the stability analysis and parameter setting method of the SADR-DPCC are elaborated, and, particularly, the impact of each parameter on the system is emphatically studied and summarized. Finally, comprehensive and comparative experiments are conducted between the proposed SADR-DPCC, conventional DPCC, ADR-DPCC, and PI. The experimental results show that the SADR-DPCC method performs better in the speed reversal performance, steady-state performance, current dynamic performance, and parameter sensitivity in the PMSM drive system. Consequently, the validity and feasibility of the SADR-DPCC for the PMSM are demonstrated.

References

[1] G. Wu, S. Huang, Q. Wu, F. Rong, C. Zhang, and W. Liao, "Robust predictive torque control of $N*3$-phase PMSM for high-power traction application," *IEEE Trans. Power Electron.*, vol. 35, no. 10, pp. 10799–10809, Oct. 2020.

[2] L. Rovere, A. Formentini, and P. Zanchetta, "FPGA implementation of a novel oversampling deadbeat controller for PMSM drives," *IEEE Trans. Ind. Electron.*, vol. 66, no. 5, pp. 3731–3741, May 2019.

[3] Z. Han and J. Liu, "Comparative analysis of vibration and noise in IPMSM considering the effect of MTPA control algorithms for electric vehicles," *IEEE Trans. Power Electron.*, vol. 36, no. 6, pp. 6850–6862, Jun. 2021.

[4] T. Wu, D. Luo, X. Wu, K. Liu, S. Huang, and X. Peng, "Square-wave voltage injection based PMSM sensorless control considering time delay at low switching frequency," *IEEE Trans. Ind. Electron.*, vol. 69, no. 6, pp. 5525–5535, Jun. 2022.

[5] M. Gu, Z. Wang, K. Yu, X. Wang, and M. Cheng, "Interleaved model predictive control for three-level neutral-point-clamped dual three-phase PMSM drives with low switching frequencies," *IEEE Trans. Power Electron.*, vol. 36, no. 10, pp. 11618–11630, Oct. 2021.

[6] X. Yuan, C. Zhang, and S. Zhang, "Torque ripple suppression for open-end winding permanent-magnet synchronous machine drives with predictive current control," *IEEE Trans. Ind. Electron.*, vol. 67, no. 3, pp. 1771–1781, Mar. 2020.

[7] X. Zhang and Z. Zhao, "Model predictive control for PMSM drives with variable dead-zone time," *IEEE Trans. Power Electron.*, vol. 36, no. 9, pp. 10514–10525, Sep. 2021.

[8] C. Ma, H. Li, X. Yao, Z. Zhang, and F. de Belie, "An improved model-free predictive current control with advanced current gradient updating mechanism," *IEEE Trans. Ind. Electron.*, vol. 68, no. 12, pp. 11968–11979, Dec. 2021.

[9] M. Siami, D. A. Khaburi, M. Rivera, and J. Rodríguez, "An experimental evaluation of predictive current control and predictive torque control for a PMSM fed by a matrix converter," *IEEE Trans. Ind. Electron.*, vol. 64, no. 11, pp. 8459–8471, Nov. 2017.

[10] X. Li, Z. Xue, L. Zhang, and W. Hua, "A low-complexity three-vector-based model predictive torque control for SPMSM," *IEEE Trans. Power Electron.*, vol. 36, no. 11, pp. 13002–13012, Nov. 2021.

[11] C. Liu and J. Shang, "Three-dimension space vector based finite control set method for OW-PMSM with zero-sequence current suppression and switching frequency reduction," *IEEE Trans. Power Electron.*, vol. 36, no. 12, pp. 14074–14086, Dec. 2021.

[12] W. Chen, S. Zeng, G. Zhang, T. Shi, and C. Xia, "A modified double vectors model predictive torque control of permanent magnet synchronous motor," *IEEE Trans. Power Electron.*, vol. 34, no. 11, pp. 11419–11428, Nov. 2019.

[13] Z. Zheng, D. Sun, M. Wang, and H. Nian, "A dual two-vector-based model predictive flux control with field-weakening operation for OW-PMSM drives," *IEEE Trans. Power Electron.*, vol. 36, no. 2, pp. 2191–2200, Feb. 2021.

[14] Y. Zhang, D. Xu, and L. Huang, "Generalized multiple-vector-based model predictive control for PMSM drives," *IEEE Trans. Ind. Electron.*, vol. 65, no. 12, pp. 9356–9366, Dec. 2018.

[15] X. Zhang and B. Hou, "Double vectors model predictive torque control without weighting factor based on voltage tracking error," *IEEE Trans. Power Electron.*, vol. 33, no. 3, pp. 2368–2380, Mar. 2018.

[16] S. Dai, J. B. Wang, Z. Sun, and E. Chong, "Deadbeat predictive current control for high-speed PMSM drives with low switching-to-fundamental frequency ratios," *IEEE Trans. Ind. Electron.*, vol. 69, no. 5, pp. 4510–4521, May 2022.
[17] X. Li, S. Zhang, C. Zhang, Y. Zhou, and C. Zhang, "An improved deadbeat predictive current control scheme for open-winding permanent magnet synchronous motors drives with disturbance observer," *IEEE Trans. Power Electron.*, vol. 36, no. 4, pp. 4622–4632, Apr. 2021.
[18] M. S. R. Saeed, W. Song, B. Yu, and X. Wu, "Low-complexity deadbeat model predictive current control with duty ratio for five-phase PMSM drives," *IEEE Trans. Power Electron.*, vol. 35, no. 11, pp. 12085–12099, Nov. 2020.
[19] C. Xu, Z. Han, and S. Lu, "Deadbeat predictive current control for permanent magnet synchronous machines with closed-form error compensation," *IEEE Trans. Power Electron.*, vol. 35, no. 5, pp. 5018–5030, May 2020.
[20] X. Yuan, C. Zhang, and S. Zhang, "A novel deadbeat predictive current control scheme for OEW-PMSM drives," *IEEE Trans. Power Electron.*, vol. 34, no. 12, pp. 11990–12000, Dec. 2019.
[21] X. Li, W. Tian, X. Gao, Q. Yang, and R. Kennel, "A generalized observer-based robust predictive current control strategy for PMSM drive system," *IEEE Trans. Ind. Electron.*, vol. 69, no. 2, pp. 1322–1332, Feb. 2022.
[22] F. Wang, D. Ke, X. Yu, and D. Huang, "Enhanced predictive model based deadbeat control for PMSM drives using exponential extended state observer," *IEEE Trans. Ind. Electron.*, vol. 69, no. 3, pp. 2357–2369, Mar. 2022.
[23] D. Ke, F. Wang, L. He, and Z. Li, "Predictive current control for PMSM systems using extended sliding mode observer with Hurwitz-based power reaching law," *IEEE Trans. Power Electron.*, vol. 36, no. 6, pp. 7223–7232, Jun. 2021.
[24] X. Zhang, B. Hou, and Y. Mei, "Deadbeat predictive current control of permanent-magnet synchronous motors with stator current and disturbance observer," *IEEE Trans. Power Electron.*, vol. 32, no. 5, pp. 3818–3834, May 2017.
[25] X. Sun, J. Cao, G. Lei, Y. Guo, and J. Zhu, "A robust deadbeat predictive controller with delay compensation based on composite sliding-mode observer for PMSMs," *IEEE Trans. Power Electron.*, vol. 36, no. 9, pp. 10742–10752, Sep. 2021.
[26] B. Wang, Z. Dong, Y. Yu, G. Wang, and D. Xu, "Static-errorless deadbeat predictive current control using second-order sliding-mode disturbance observer for induction machine drives," *IEEE Trans. Power Electron.*, vol. 33, no. 3, pp. 2395–2403, Mar. 2018.
[27] M. Yang, X. Lang, J. Long, and D. Xu, "Flux immunity robust predictive current control with incremental model and extended state observer for PMSM drive," *IEEE Trans. Power Electron.*, vol. 32, no. 12, pp. 9267–9279, Dec. 2017.
[28] L. He, F. Wang, J. Wang, and J. Rodríguez, "Zynq implemented Luenberger disturbance observer based predictive control scheme for PMSM drives," *IEEE Trans. Power Electron.*, vol. 35, no. 2, pp. 1770–1778, Feb. 2020.
[29] X. Yuan, Y. Zuo, Y. Fan, and C. H. T. Lee, "Model-free predictive current control of SPMSM drives using extended state observer," *IEEE Trans. Ind. Electron.*, vol. 69, no. 7, pp. 6540–6550, Jul. 2022.
[30] X. An, G. Liu, Q. Chen, W. Zhao, and X. Song, "Robust predictive current control for fault-tolerant operation of five-phase PM motors based on online stator inductance identification," *IEEE Trans. Power Electron.*, vol. 36, no. 11, pp. 13162–13175, Nov. 2021.
[31] J. Li, Y. Xia, X. Qi, and Z. Gao, "On the necessity, scheme, and basis of the linear-nonlinear switching in active disturbance rejection control," *IEEE Trans. Ind. Electron.*, vol. 64, no. 2, pp. 1425–1435, Feb. 2017.
[32] C. Gong, Y. Hu, M. Ma, L. Yan, J. Liu, and H. Wen, "Accurate FCS model predictive current control technique for surface-mounted PMSMs at low control frequency," *IEEE Trans. Power Electron.*, vol. 35, no. 6, pp. 5567–5572, Jun. 2020.
[33] A. D. Alexandrou, N. K. Adamopoulos, and A. G. Kladas, "Development of a constant switching frequency deadbeat predictive control technique for field-oriented synchronous permanent-magnet motor drive," *IEEE Trans. Ind. Electron.*, vol. 63, no. 8, pp. 5167–5175, Aug. 2016.
[34] P. Lin, Z. Wu, K.-Z. Liu, and X.-M. Sun, "A class of linear-nonlinear switching active disturbance rejection speed and current controllers for PMSM," *IEEE Trans. Power Electron.*, vol. 36, no. 12, pp. 14366–14382, Dec. 2021.
[35] Z. Hao et al., "Linear/nonlinear active disturbance rejection switching control for permanent magnet synchronous motors," *IEEE Trans. Power Electron.*, vol. 36, no. 8, pp. 9334–9347, Aug. 2021.
[36] P. Li, G. Zhu, and M. Zhang, "Linear active disturbance rejection control for servo motor systems with input delay via internal model control rules," *IEEE Trans. Ind. Electron.*, vol. 68, no. 2, pp. 1077–1086, Feb. 2021.

Zhengjie Hao received the B.S. degree in electrical engineering and automation and the M.S. degree in electrical engineering from Jiangsu University, Zhenjiang, China, in 2016 and 2019, respectively, and the Ph.D. degree in applied physics from Jilin University, Jilin, China, in 2022.

He is currently an Associate Professor with the School of Electrical and Information Engineering, Northeast Petroleum University, Daqing, China. His research interests include robust control technology for permanent magnet synchronous motors.

Yang Yang received the Ph.D. degree in vehicle engineering from Jilin University, Changchun, China, in 2018.

He is currently an Associate Professor with the College of Physics, Jilin University. His research interests include power electronics and control of permanent magnet synchronous motors.

Keyong Shao received the B.S. degree in production process automation from Daqing Northeast Petroleum Institute, Daqing, China, in 1992, and the M.S. and Ph.D. degrees in control theory and control engineering from Northeast University, Shenyang, China, in 2000 and 2003, respectively.

He is currently a Professor with the School of Electrical and Information Engineering, Northeast Petroleum University. His research interests include robust control and fractional-order system theory.

Yuanhong Liu received the Ph.D. degree in control theory and control engineering from the Department of Control Science and Engineering, Harbin Institute of Technology, Harbin, China, in 2016.

He is currently an Associate Professor with the School of Electrical and Information Engineering, Northeast Petroleum University, Shenyang, China. His research interests include nonlinear dimension reduction, machine learning and pattern recognition, and signal processing.